

Supplementary Information

Benzylidene-Directed Glycosylations – Mechanistic Insights from Cryogenic Infrared Spectroscopy

Chun-Wei Chang,^{1,2,†} Kim Greis,^{1,2,†} Carla Kirschbaum,^{1,2} Sabrina Lechnitz,^{1,3} Gerard Meijer,² Gert von Helden,² Peter H. Seeberger,^{1,3} Kevin Pagel^{*1,2}

¹ Freie Universität Berlin, Institute of Chemistry and Biochemistry, Berlin, Germany

² Fritz Haber Institute of the Max Planck Society, Berlin, Germany

³ Max Planck Institute of Colloids and Interfaces, Potsdam, Germany

†Authors contributed equally.

Correspondence to: Prof. Dr. Kevin Pagel

kevin.pagel@fu-berlin.de

1.	Mass Spectrometry and Infrared Spectroscopy	1
1.1	Experimental Setup.....	1
1.2	Infrared Spectra	3
1.3	Mass Spectra.....	4
2.	Computational Methods	6
2.1	Method Description	6
2.2	Energetics of Intermediates in Vacuum	7
2.3	Energy Hierarchies of Intermediates in Vacuum	10
2.4	3D Structures of Intermediates in Vacuum.....	12
2.5	Energetics of Intermediates Using a Solvent Model.....	15
2.6	Energy Hierarchies of Intermediates Using a Solvent Model	16
2.7	3D Structures of Intermediates in Different Solvents	20
2.8	xyz-Coordinates of Reoptimized Structures	26
3.	Experimental Details	27
3.1	Materials.....	27
3.2	Probing the Stereoselectivity of 4,6- <i>O</i> -Benzylidene-Directed Glycosylation.....	28
	References	31

1. Mass Spectrometry and Infrared Spectroscopy

1.1 Experimental Setup

The precursors were dissolved in a 9:1 (V:V) mixture of acetonitrile and water to yield 0.1 mM solutions. Pd/Pt coated glass capillaries (Sputter Coater HR 208, *Cressington*) for nano electrospray ionization (nESI) are pulled to a tip with an inner diameter of 1–2 μm using a micropipette puller (Model P-1000, *Sutter Instrument*).

Glycosyl cations were generated and probed using a custom-built helium droplet instrument (Figure S1). Glycosyl cations are formed after nESI (Z-spray) with a voltage of 1.1 kV to the tip of the capillary of the precursors, followed by in-source fragmentation of the generated ions. Commonly, nESI of the precursor leads to sodiated and protonated ions, whereas in-source fragmentation can lead to the cleavage of labile leaving groups, such as SET.

After passing through two ring-electrode ion guides, the ions of interest are mass-to-charge selected by a quadrupole mass filter. Then, the ions enter a quadrupole bender. If no voltage is applied, the ions directly pass through the bender to get to a time-of-flight detector to record mass spectra (Figures S3-S5) and to monitor the ion signal. If ± 33 V are applied to rods of the quadrupole bender, the ions are bent and enter a hexapole ion trap that is cooled to 90 K by liquid nitrogen in this experiment. The ions of interest are subsequently accumulated in the ion trap and thermalized by collisions with helium buffer gas.

Expansion of pressurized helium into the vacuum by a pulsed Even-Lavie valve leads to the formation of a beam of superfluid helium nanodroplets (0.4 K) that is traversing the ion trap, picking up ions, rapidly cooling them to their equilibrium temperature, and guiding them to the detection region. Here, an infrared (IR) beam generated by the Fritz Haber Institute free-electron laser (FHI FEL¹) overlaps with the ion beam. Upon the absorption of resonant photons, vibrational modes of the molecular ions are excited. The ions dissipate the energy to the helium matrix to get back to their ground state. After the absorption of multiple photons, the probed ions are released from the helium nanodroplets and detected by a time-of-flight detector. The ion yield can be plotted as a function of the IR wavenumber, leading to an IR spectrum (Figures 2, 3 and S2). Due to the multiphoton absorption process, the intensities in the obtained IR spectrum do not scale linearly. As a first-order correction, the ion signal is divided by the energy of the IR macropulse.

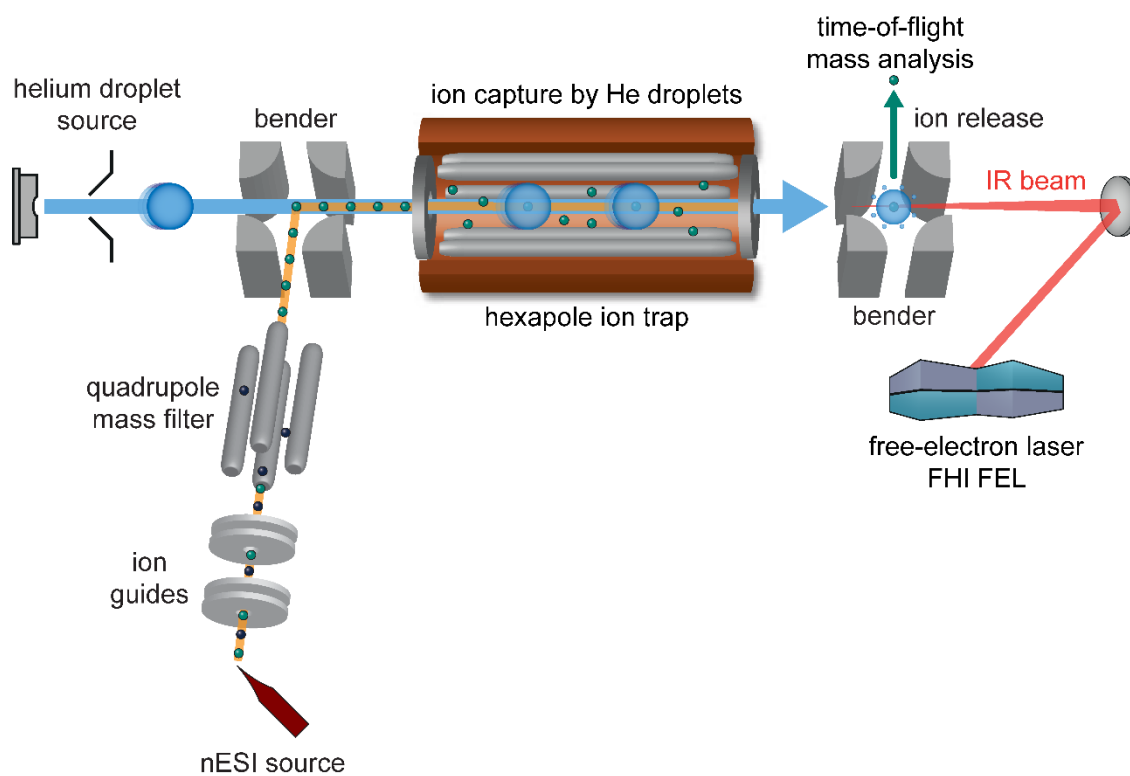
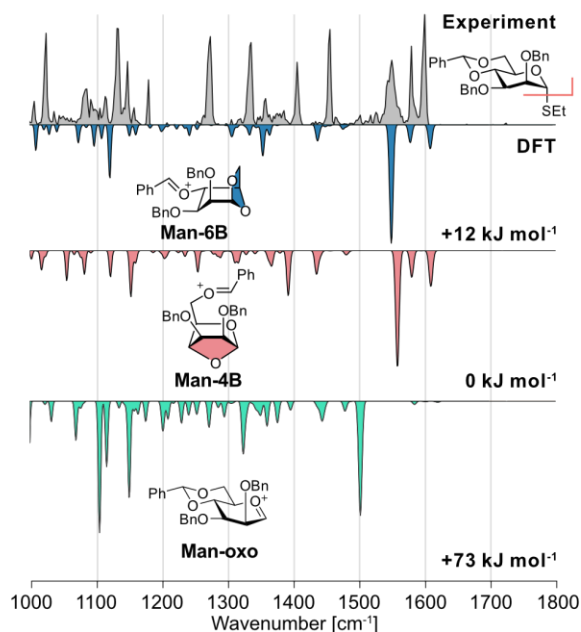


Figure S1. Schematic drawing of the custom-built helium droplet instrument combining mass spectrometry and infrared spectroscopy in helium droplets to probe mass-to-charge selected ions.

1.2 Infrared Spectra

a. Cryogenic Infrared spectroscopy of Mannosyl Cations



b. Cryogenic Infrared spectroscopy of Galactosyl Cations

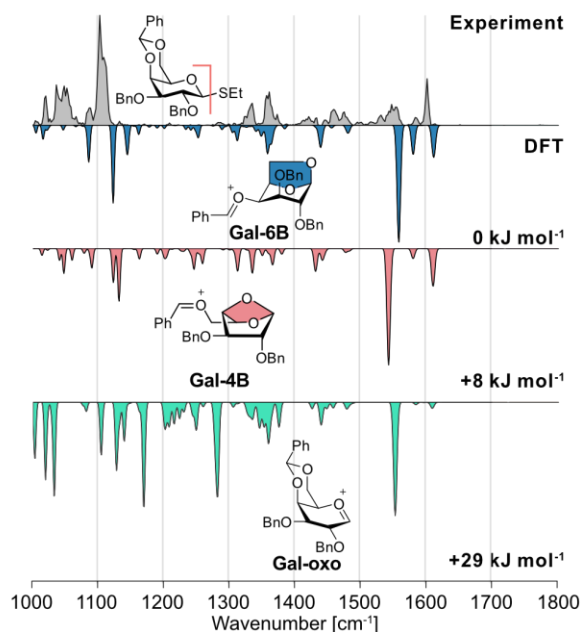


Figure S2. Cryogenic infrared spectra of glycosyl cations ($m/z = 431$) generated from **Man-SEt** and **Gal-SEt** precursors individually. The experimental cryogenic IR spectrum is shown as a gray trace, whereas computed spectra of the lowest-energy 1,6-anhydro cation (blue), 1,4-anhydro cation (red) and oxocarbenium ion (green) for (a) mannosyl and (b) galactosyl cations are shown in the inverted traces below.

1.3 Mass Spectra

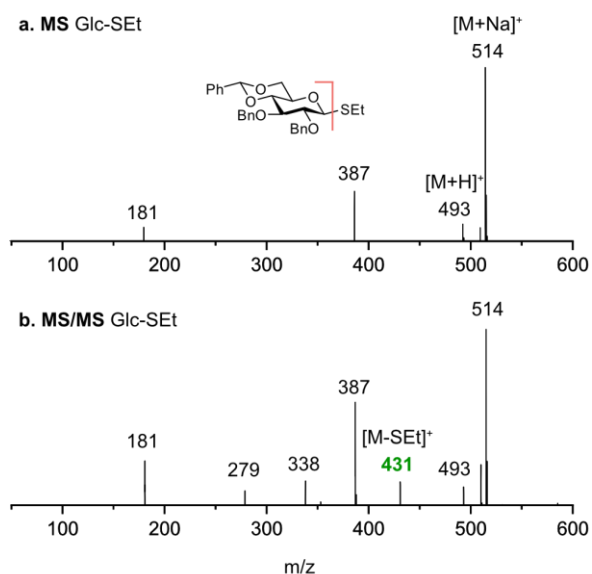


Figure S3. Mass spectra of precursors of (a) Ethyl 2,3-di-*O*-benzyl-4,6-*O*-benzylidene-D-thioglucofuranoside (**Glc-SEt**) recorded on the helium droplet instrument. (b) In-source fragmentation of precursor ions $[M+H]^+$ ($m/z = 493$) and $[M+Na]^+$ ($m/z = 514$) leads to galactosyl cations ($m/z = 431$).

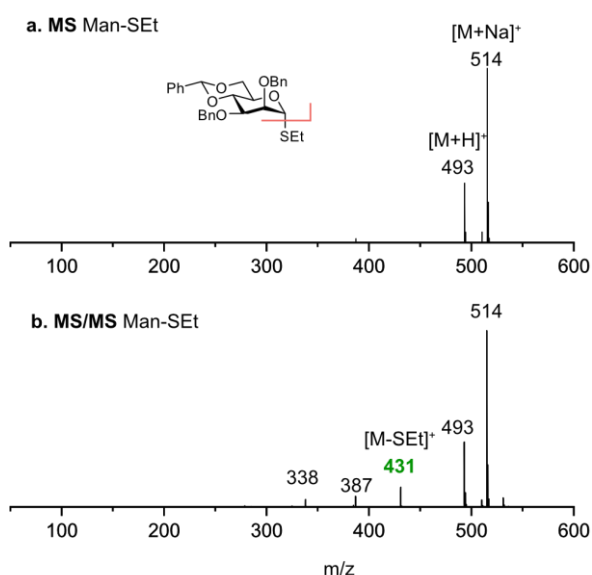


Figure S4. Mass spectra of precursors of (a) Ethyl 2,3-di-*O*-benzyl-4,6-*O*-benzylidene-D-thiomannopyranoside (**Man-SEt**) recorded on the helium droplet instrument. (b) In-source fragmentation of precursor ions $[M+H]^+$ ($m/z = 493$), and $[M+Na]^+$ ($m/z = 514$) leads to galactosyl cations ($m/z = 431$).

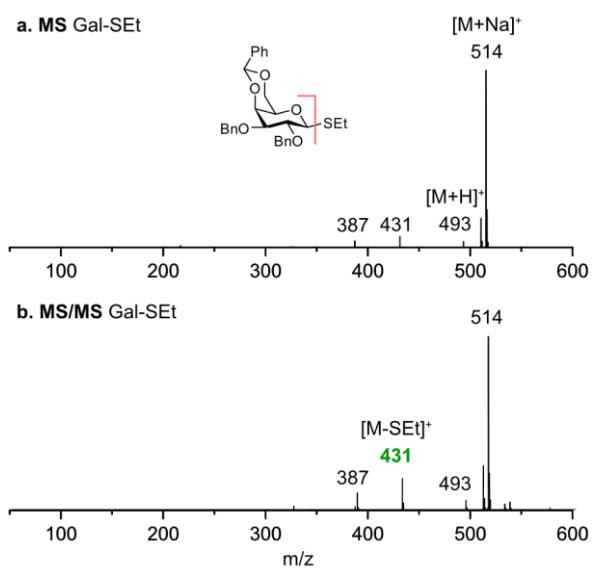


Figure S5. Mass spectra of precursors of (a) Ethyl 2,3-di-*O*-benzyl-4,6-*O*-benzylidene-D-thiogalactopyranoside (**Gal-SEt**) recorded on the helium droplet instrument. (b) In-source fragmentation of precursor ions $[M+H]^+$ ($m/z = 493$), and $[M+Na]^+$ ($m/z = 514$) leads to galactosyl cations ($m/z = 431$).

2. Computational Methods

2.1 Method Description

Initial geometries of glycosyl cations candidates (**Glc-oxo**, **Glc-4B**, **Glc-6B**, **Man-oxo**, **Man-4B**, **Man-6B**, **Gal-oxo**, **Gal-4B**, **Gal-6B**) were constructed by chemical intuition using GaussView 6.² Conformational search were performed using CREST³ with the semiempirical method GFN2-xTB⁴ using default settings. The selected structures are reoptimized and their harmonic frequencies are computed at the PBE1PBE/6-311+G(d,p) EmpiricalDispersion=GD3BJ^{5,6} level of theory using Gaussian 16.² Relative free energies at 90 K (approximate temperature of the ion trap) were extracted from the frequency calculation and are represented with the energy ΔE (including zero-point vibrational energy) in the tables and figures below.

2.2 Energetics of Intermediates in Vacuum

Table S1. List of conformations of glucosyl (Glc) cations optimized at PBE1PBE/6-311+G(d,p) EmpiricalDispersion=GD3BJ level of theory. Relative energies (ΔE , including zero-point vibrational energy), and free energies (ΔF) at 90 K are assigned to each conformer. †The lowest-free energy conformer and its simulated IR spectra are showed highlighted in the manuscript or SI.

Glycosyl cations/conformer	ΔE (kJ mol ⁻¹)	ΔF (kJ mol ⁻¹)
Glc-oxo/conf_1†	72.0883535	72.80242962
Glc-oxo/conf_2	73.4116055	74.23188162
Glc-oxo/conf_3	78.4578165	77.58998814
Glc-oxo/conf_4	81.427257	82.21266148
Glc-oxo/conf_5	95.316152	93.92049379
Glc-oxo/conf_6	99.5983425	100.4582455
Glc-oxo/conf_7	102.5021455	103.2495082
Glc-oxo/conf_8	104.767952	105.0596057
Glc-6B/conf_1†	0	0
Glc-6B/conf_2	5.6894585	5.319343575
Glc-6B/conf_3	7.0809735	5.968251113
Glc-6B/conf_4	13.363795	12.04580545
Glc-6B/conf_5	17.06575	16.85572761
Glc-4B/conf_1†	28.9461375	27.58852108
Glc-4B/conf_2	35.9614735	35.44632425
Glc-4B/conf_3	38.726125	39.257125
Glc-4B/conf_4	41.79796	40.9887794
Glc-4B/conf_5	44.565237	43.41447282
Glc-4B/conf_6	50.840182	49.96046558
Glc-4B/conf_7	63.657873	63.00402972

Table S2. List of conformations of galactosyl (Gal) cations optimized at PBE1PBE/6-311+G(d,p) EmpiricalDispersion=GD3BJ level of theory. Relative energies (ΔE , including zero-point vibrational energy), and free energies (ΔF) at 90 K are assigned to each conformer. †The lowest-free energy conformer and its simulated IR spectra are showed highlighted in the manuscript or SI.

Glycosyl cations/conformer	ΔE (kJ mol ⁻¹)	ΔF (kJ mol ⁻¹)
Gal-oxo/conf_1†	29.5500025	28.78361892
Gal-oxo/conf_2	32.367164	32.04380878
Gal-oxo/conf_3	42.065761	41.62590279
Gal-oxo/conf_4	43.1605945	43.60837808
Gal-oxo/conf_5	57.7163665	58.55724859
Gal-6B/conf_1†	0	0
Gal-6B/conf_2	4.0353935	2.554933799
Gal-6B/conf_3	6.3248295	6.169492187
Gal-6B/conf_4	14.266967	12.05341028
Gal-6B/conf_5	19.554724	14.37152997
Gal-6B/conf_6	20.352876	17.75969391
Gal-6B/conf_7	21.098518	19.28440009
Gal-6B/conf_8	28.6783365	28.45563351
Gal-6B/conf_9	34.168257	33.52550924
Gal-4B/conf_1†	9.4911825	7.822098918
Gal-4B/conf_2	11.3762915	8.907537769
Gal-4B/conf_3	12.261085	10.4897641
Gal-4B/conf_4	15.936785	12.68975963
Gal-4B/conf_5	23.403707	22.19270998
Gal-4B/conf_6	26.3889005	24.36079751

Table S3. List of conformations of mannosyl (Man) cations optimized at PBE1PBE/6-311+G(d,p) EmpiricalDispersion=GD3BJ level of theory. Relative energies (ΔE , including zero-point vibrational energy), and free energies (ΔF) at 90 K are assigned to each conformer. †The lowest-free energy conformer and its simulated IR spectra are showed highlighted in the manuscript or SI.

Glycosyl cations/conformer	ΔE (kJ mol ⁻¹)	ΔF (kJ mol ⁻¹)
Man-oxo/conf_1†	72.353529	72.99548422
Man-oxo/conf_2	79.2087095	78.10311995
Man-oxo/conf_3	86.9434325	86.08352951
Man-oxo/conf_4	93.268262	94.11865454
Man-oxo/conf_5	100.7220565	100.5564162
Man-6B/conf_1†	13.153755	12.32238336
Man-6B/conf_2	24.264871	24.03820533
Man-4B/conf_1†	0	0
Man-4B/conf_2	5.7472195	7.799098604
Man-4B/conf_3	7.283137	9.08536685
Man-4B/conf_4	12.051045	12.90223007
Man-4B/conf_5	15.2279	15.65587015
Man-4B/conf_6	19.959051	20.04226742
Man-4B/conf_7	27.893312	29.13284036
Man-4B/conf_8	34.005476	35.23390884

2.3 Energy Hierarchies of Intermediates in Vacuum

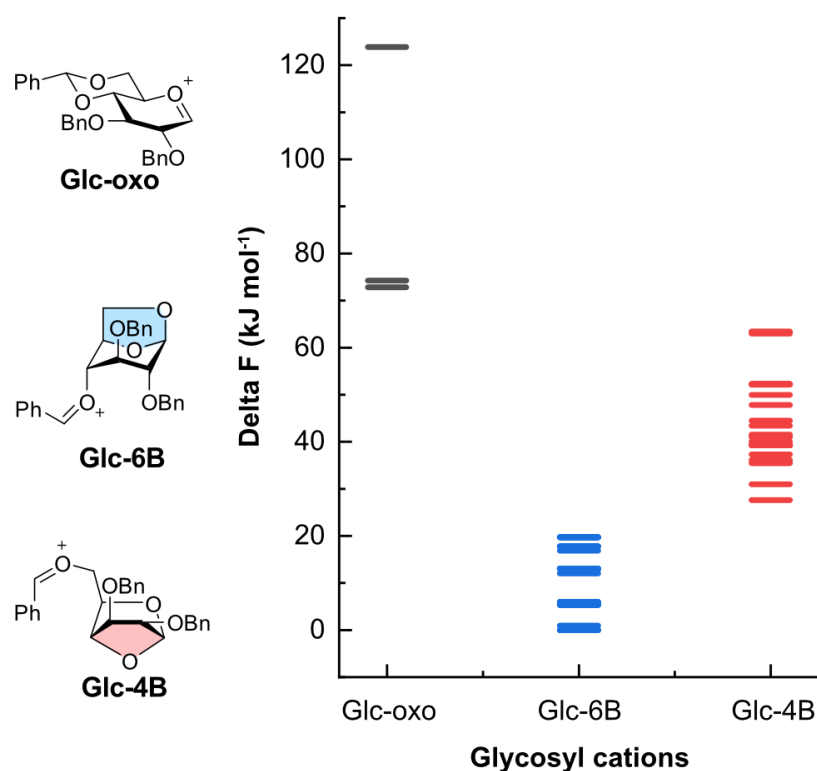


Figure S6. Energy hierarchies of the reoptimized structures for glucosyl cations.

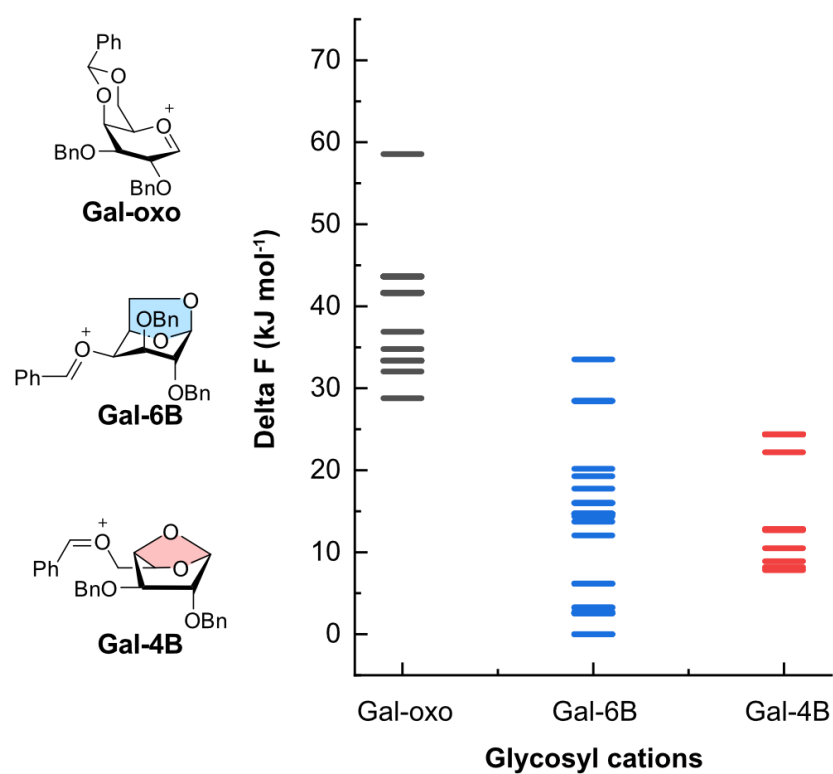


Figure S7. Energy hierarchies of the reoptimized structures for galactosyl cations.

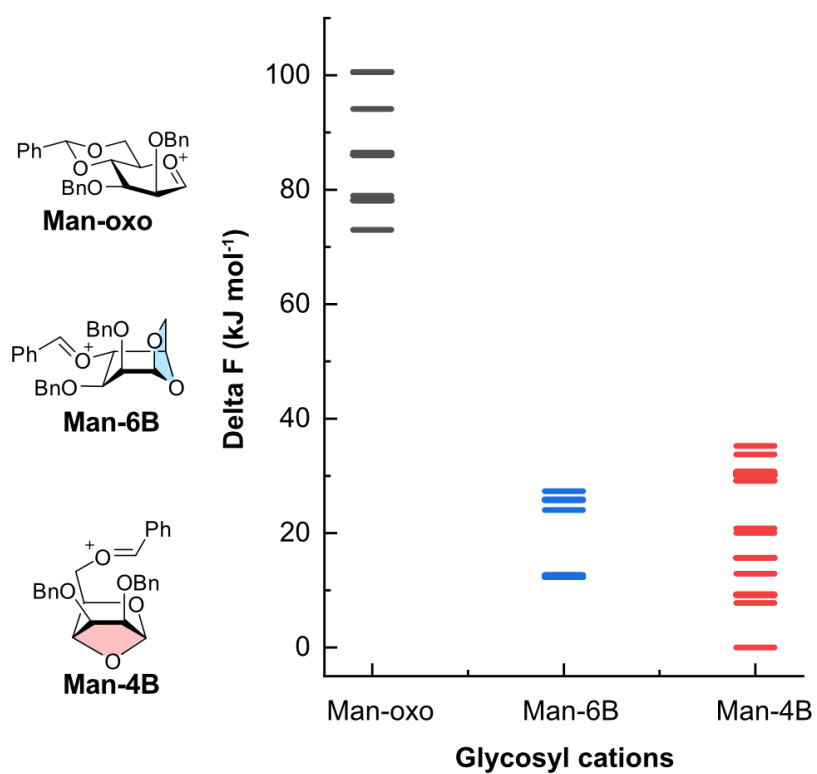
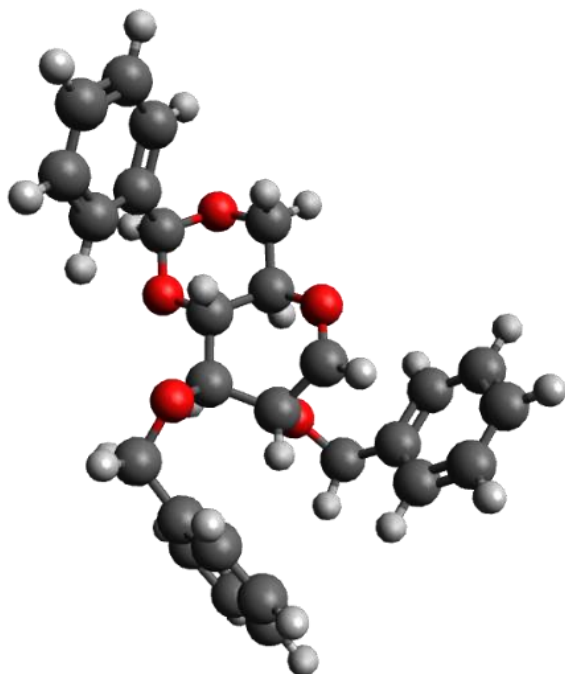


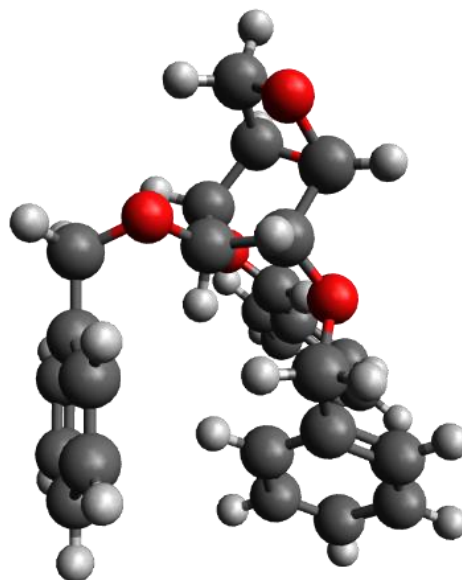
Figure S8. Energy hierarchies of the reoptimized structures for mannosyl cations.

2.4 3D Structures of Intermediates in Vacuum

a.



b.



c.

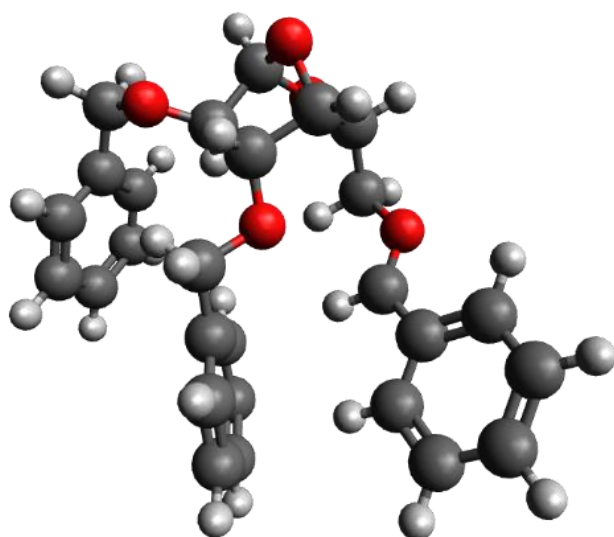


Figure S9. Reoptimized geometries of glucosyl (Glc) cations. The structures correspond to those that are highlighted with a dagger (†) in Tables S1. a) **Glc-oxo**, b) **Glc-6B**, and c) **Glc-4B**.

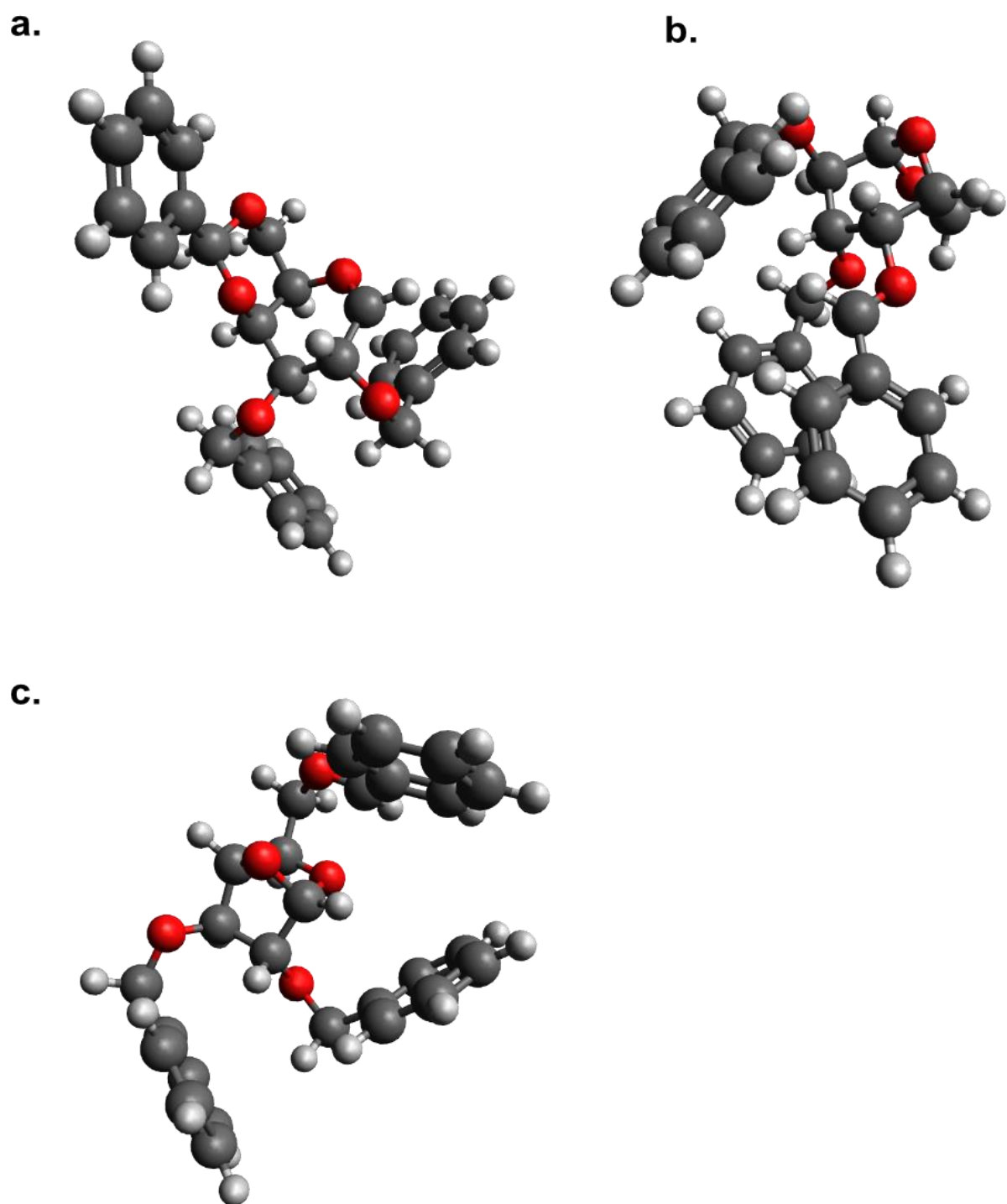
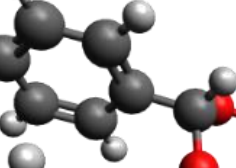


Figure S10. Reoptimized geometries of galactosyl (Gal) cations. The structures correspond to those that are highlighted with a dagger (†) in Tables S2. a) **Gal-oxo**, b) **Gal-6B**, and c) **Gal-4B**.



A 3D ball-and-stick model of a complex organic molecule, possibly a protein-ligand complex. The structure features a central core with various side chains. A prominent red oxygen atom is visible, likely part of a carbonyl or hydroxyl group. The model uses grey for carbon, white for hydrogen, and red for oxygen atoms. The overall shape is elongated and somewhat irregular, with several branching points.

4B.

2.5 Energetics of Intermediates Using a Solvent Model

Table S4. List of the most stable conformer of glycosyl cations (**Glc-4B** and **Glc-6B**) optimized at the PBE0+D3/6-311+G(d,p) level of theory using the COSMO solvation model^{7,8} for various solvents with distinct relative permittivities (ϵ_r). Relative free energies (ΔF) at 298 K are assigned to each conformer and compared to the most stable structure of **Glc-oxo** ($\Delta F = 0$) in the corresponding solvent system. The corresponding structures of are shown in the SI.

Structure	Solvent								
	<i>Vacuum</i>	Dioxane	Toluene	Et ₂ O	CHCl ₃	DCM	ACN	DMSO	H ₂ O
Glc-4B	-50.0053	-42.2390	-42.9427	-45.2662	-48.1989	-47.8366	-47.4113	-48.7057	-44.3027
Glc-6B	-74.4539	-69.4707	-69.1583	-70.4159	-70.4842	-65.2463	-62.3162	-64.1646	-59.6802

Table S5. List of the most stable conformer of mannosyl cations (**Man-4B** and **Man-6B**) optimized at the PBE0+D3/6-311+G(d,p) level of theory using the COSMO solvation model^{7,8} for various solvents with distinct relative permittivities (ϵ_r). Relative free energies (ΔF) at 298 K are assigned to each conformer and compared to the most stable structure of **Man-oxo** ($\Delta F = 0$) in the corresponding solvent system. The corresponding structures of are shown in the SI.

Structure	Solvent								
	<i>Vacuum</i>	Dioxane	Toluene	Et ₂ O	CHCl ₃	DCM	ACN	DMSO	H ₂ O
Man-4B	-74.4802	-58.0052	-63.1932	-66.5853	-64.7816	-61.8568	-60.4285	-59.8640	-59.7721
Man-6B	-64.0806	-65.3776	-65.9342	-61.4813	-59.4492	-57.6770	-59.5647	-56.1069	-55.7026

Table S6. List of the most stable conformer of galactosyl cations (**Gal-4B** and **Gal-6B**) optimized at the PBE0+D3/6-311+G(d,p) level of theory using the COSMO solvation model^{7,8} for various solvents with distinct relative permittivities (ϵ_r). Relative free energies (ΔF) at 298 K are assigned to each conformer and compared to the most stable structure of **Gal-oxo** ($\Delta F = 0$) in the corresponding solvent system. The corresponding structures of are shown in the SI.

Structure	Solvent								
	<i>Vacuum</i>	Dioxane	Toluene	Et ₂ O	CHCl ₃	DCM	ACN	DMSO	H ₂ O
Gal-4B	-23.8185	-19.0585	-23.3381	-22.1251	-20.9856	-24.3961	-19.0086	-22.6318	-21.9781
Gal-6B	-27.8802	-23.9131	-28.9488	-25.9452	-25.1943	-25.8953	-22.6974	-26.8169	-26.0476

2.6 Energy Hierarchies of Intermediates Using a Solvent Model

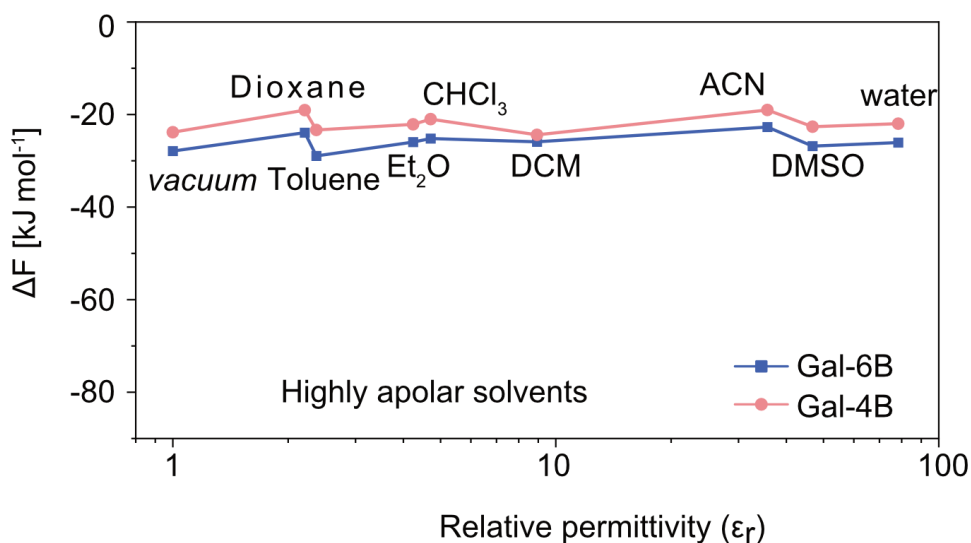


Figure S12. Relative stabilities of rearranged galactosyl cations using a solvent model. The free energies of the most stable conformers of **Gal-6B** (blue) and **Gal-4B** (red) were calculated with a solvent model for different solvents relative to **Gal-oxo** ($\Delta F = 0$). **Gal-6B** and **Gal-4B** are similarly thermodynamically stabilized for different solvents.

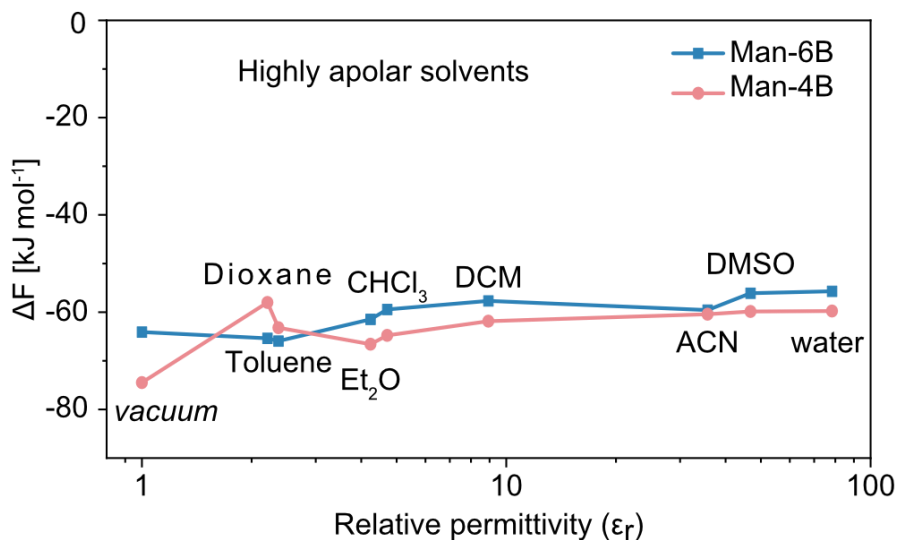


Figure S13. Relative stabilities of rearranged galactosyl cations using a solvent model. The free energies of the most stable conformers of **Man-6B** (blue) and **Man-4B** (red) were calculated with a solvent model for different solvents relative to **Man-oxo** ($\Delta F = 0$). **Man-6B** and **Man-4B** are similarly thermodynamically stabilized for different solvents.

Influence of the Surrounding Medium in Glc at 298 K

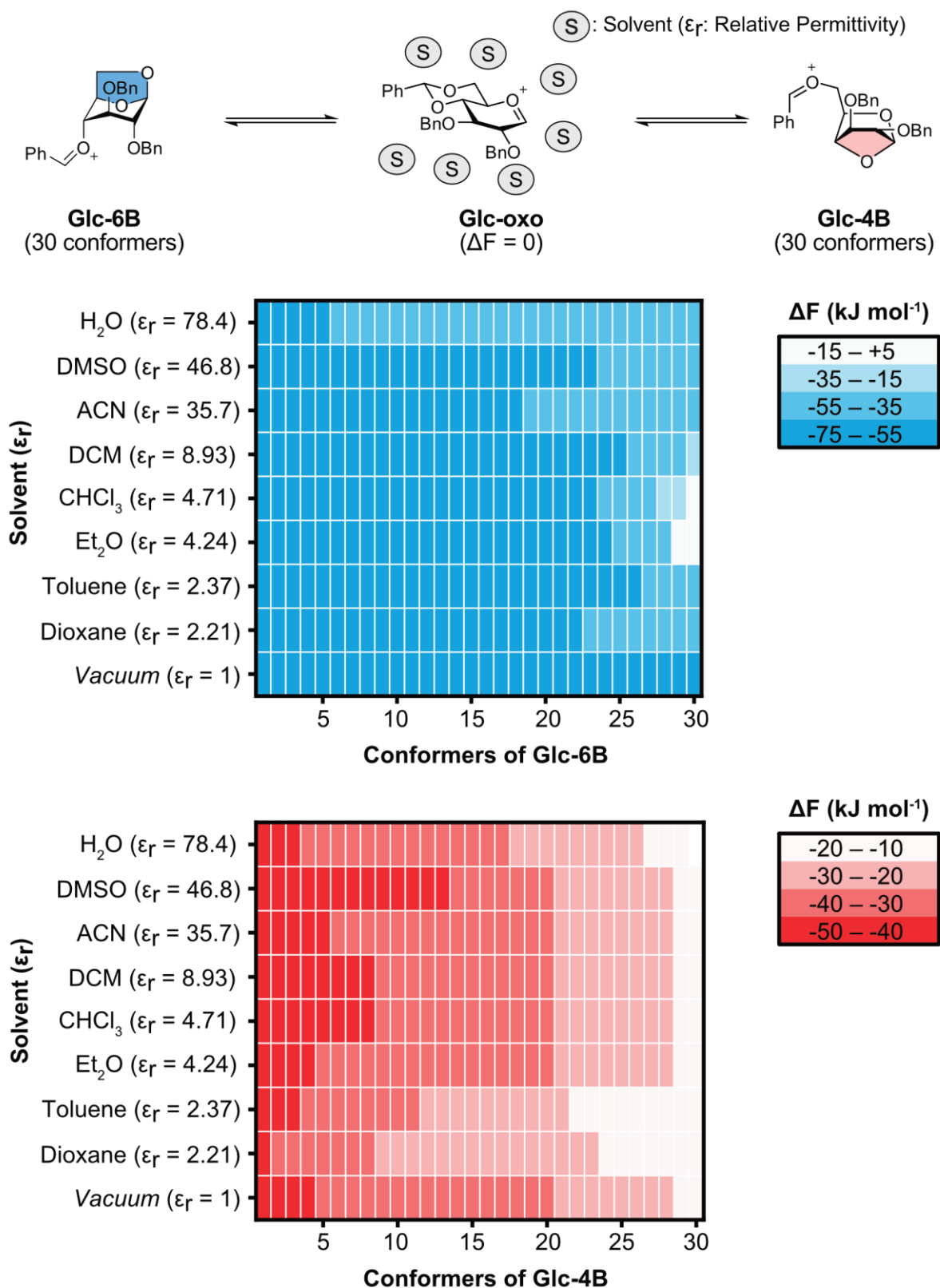


Figure S14. 30 conformers of **Glc-6B** (blue) and **Glc-4B** (red) were optimized with a solvent model for different solvents and their relative energies of each conformer relative to **Glc-oxo** are shown.

Influence of the Surrounding Medium in Gal at 298 K

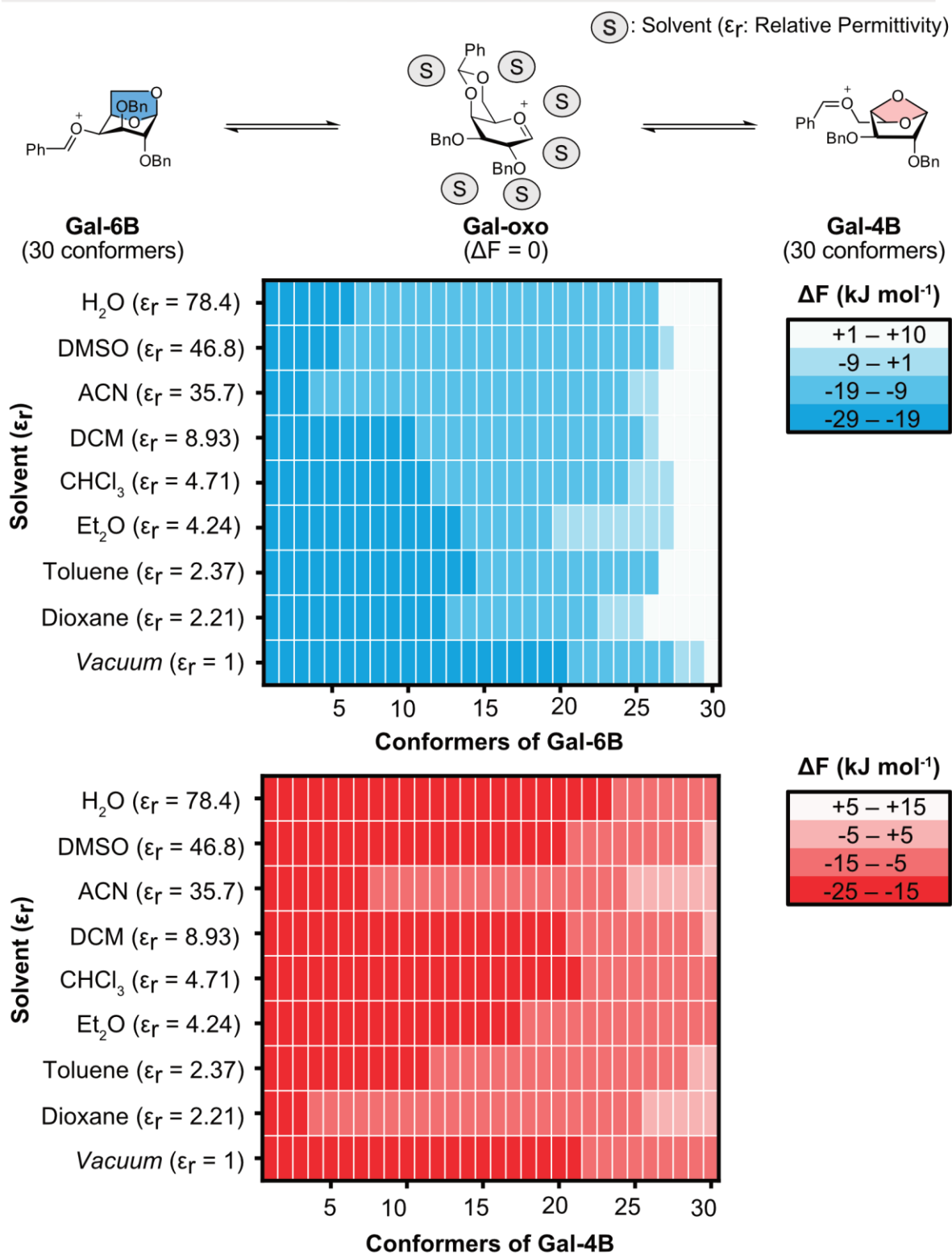


Figure S15. 30 conformers of **Gal-6B** (blue) and **Gal-4B** (red) were calculated with a solvent model for different solvents, and the relative energies of each conformer against **Gal-oxo** are shown.

Influence of the Surrounding Medium in Glc at 298 K

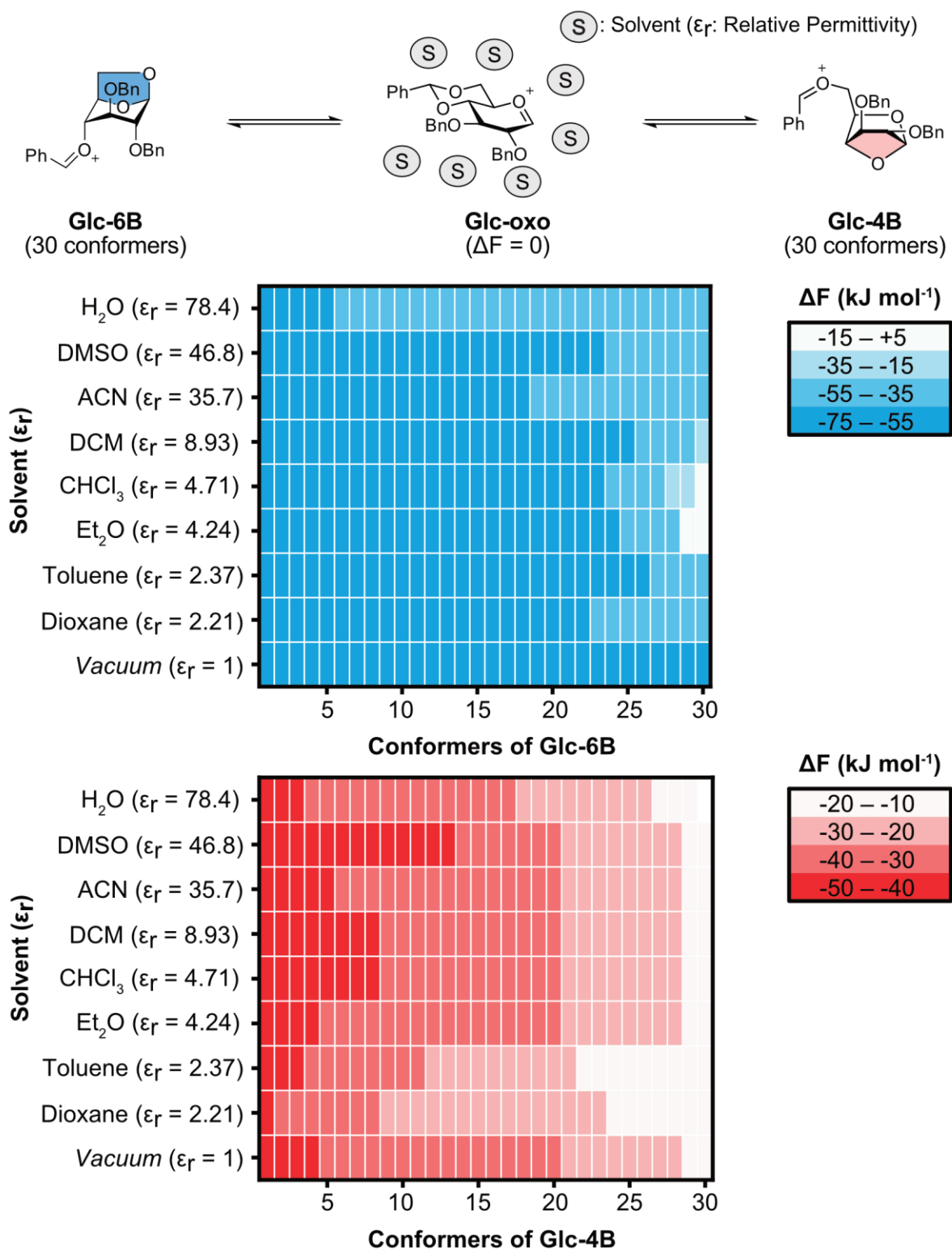
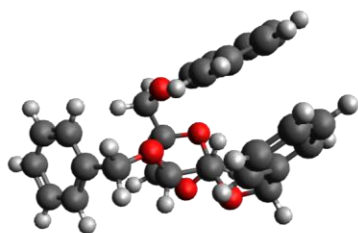


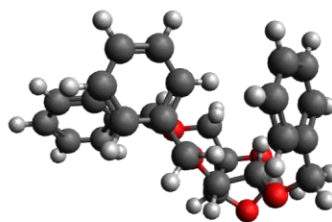
Figure S16. 30 conformers of **Man-6B** (blue) and **Man-4B** (red) were calculated with a solvent model for different solvents and their relative energies of each conformer against **Man-oxo** are shown.

2.7 3D Structures of Intermediates in Different Solvents

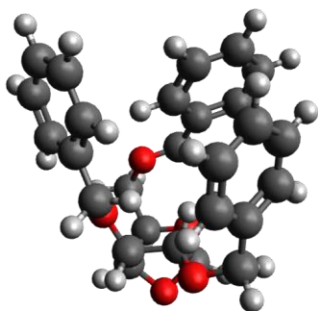
A.



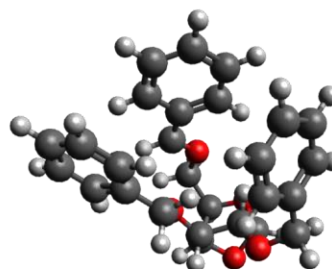
B.



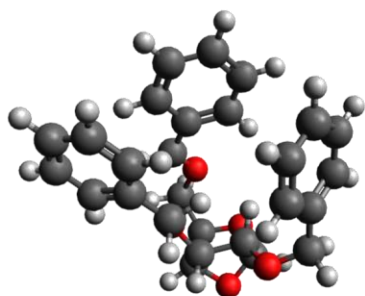
C.



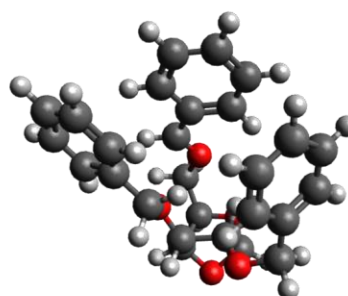
D.



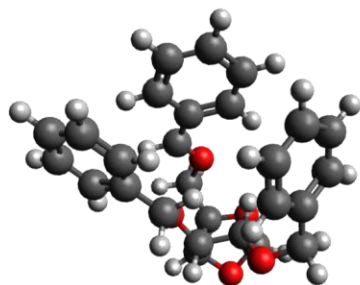
E.



F.



G.



H.

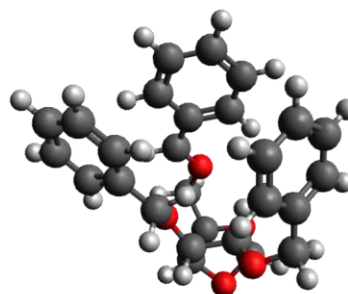


Figure S17. Reoptimized geometries of **Glc-4B** using a solvent model with different solvents. The structures correspond to those that are highlighted in entry 1, Table S4. A) 1,4-Dioxane. B) Toluene. C) Et₂O. D) CHCl₃. E) DCM. F) ACN. G) DMSO. H) Water.

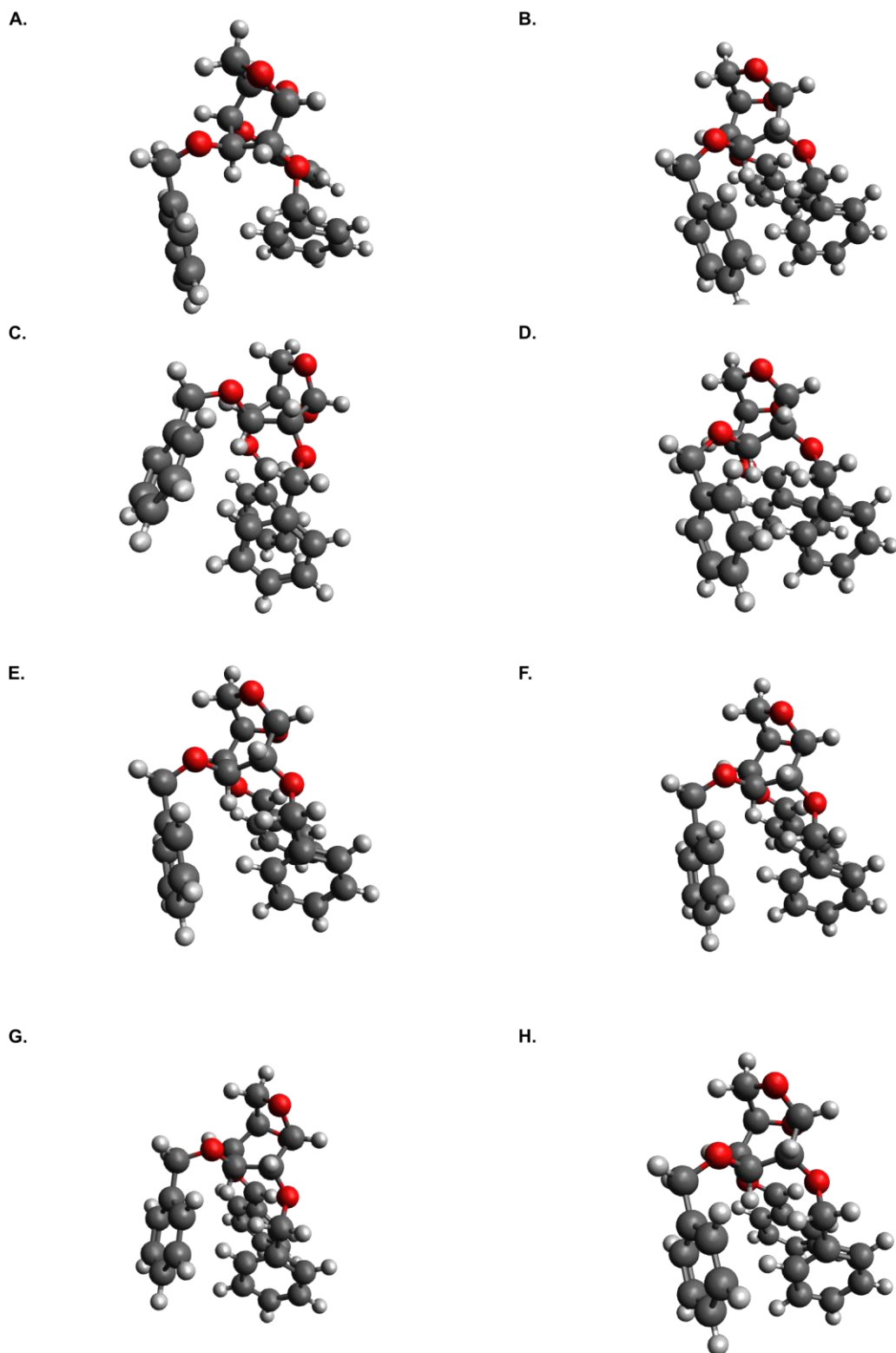


Figure S18. Reoptimized geometries of **Glc-6B** within different surrounding medias (solvents). The structures correspond to those that are highlighted in entry 1, **Error! Reference source not found.** A) 1,4-Dioxane. B) Toluene. C) Et₂O. D) CHCl₃. E) DCM. F) ACN. G) DMSO. H) Water.

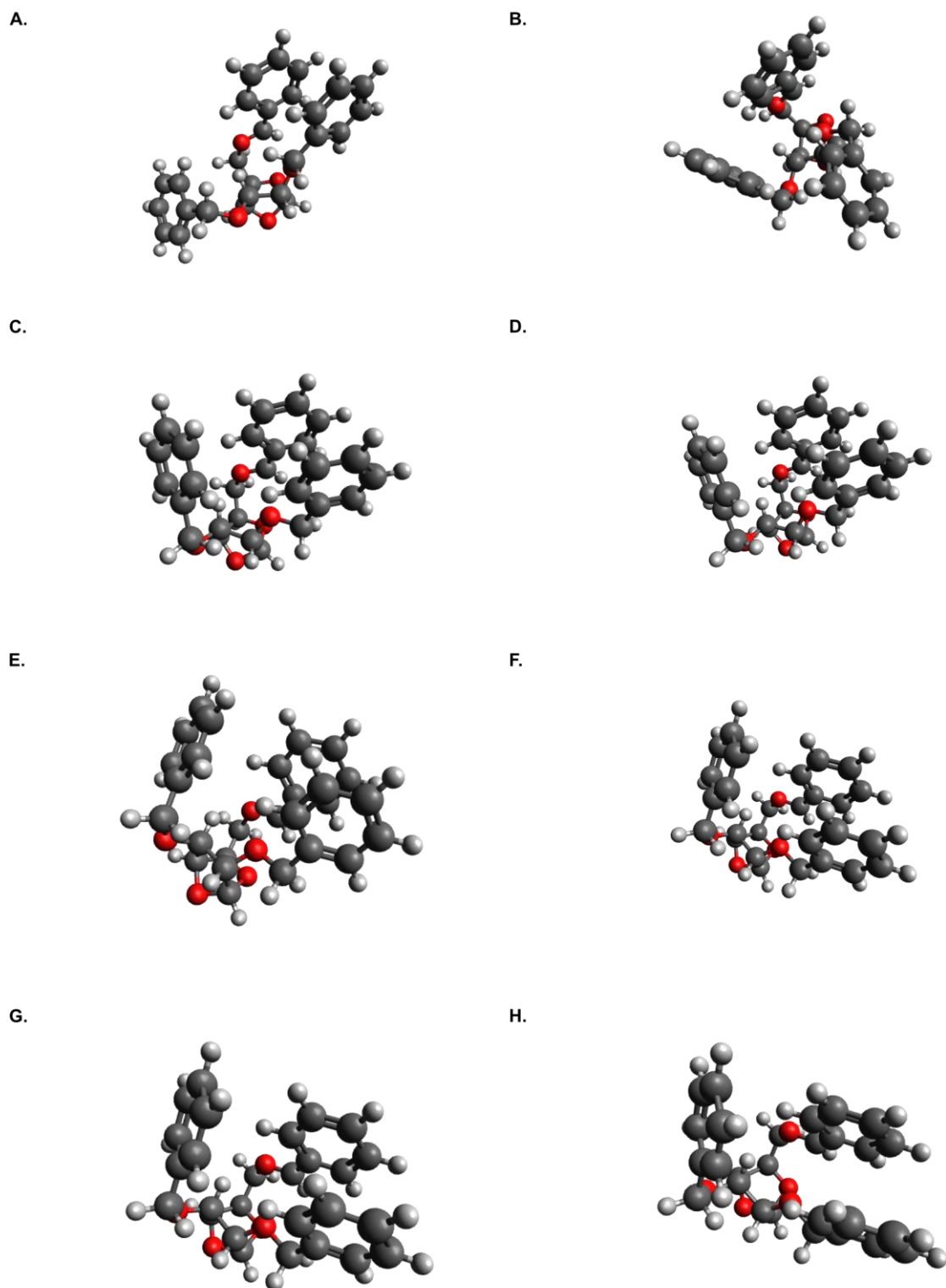


Figure S19. Reoptimized geometries of **Man-4B** within different surrounding medias (solvents). The structures correspond to those that are highlighted in entry 1, **Table S5**. A) 1,4-Dioxane. B) Toluene. C) Et₂O. D) CHCl₃. E) DCM. F) ACN. G) DMSO. H) Water.

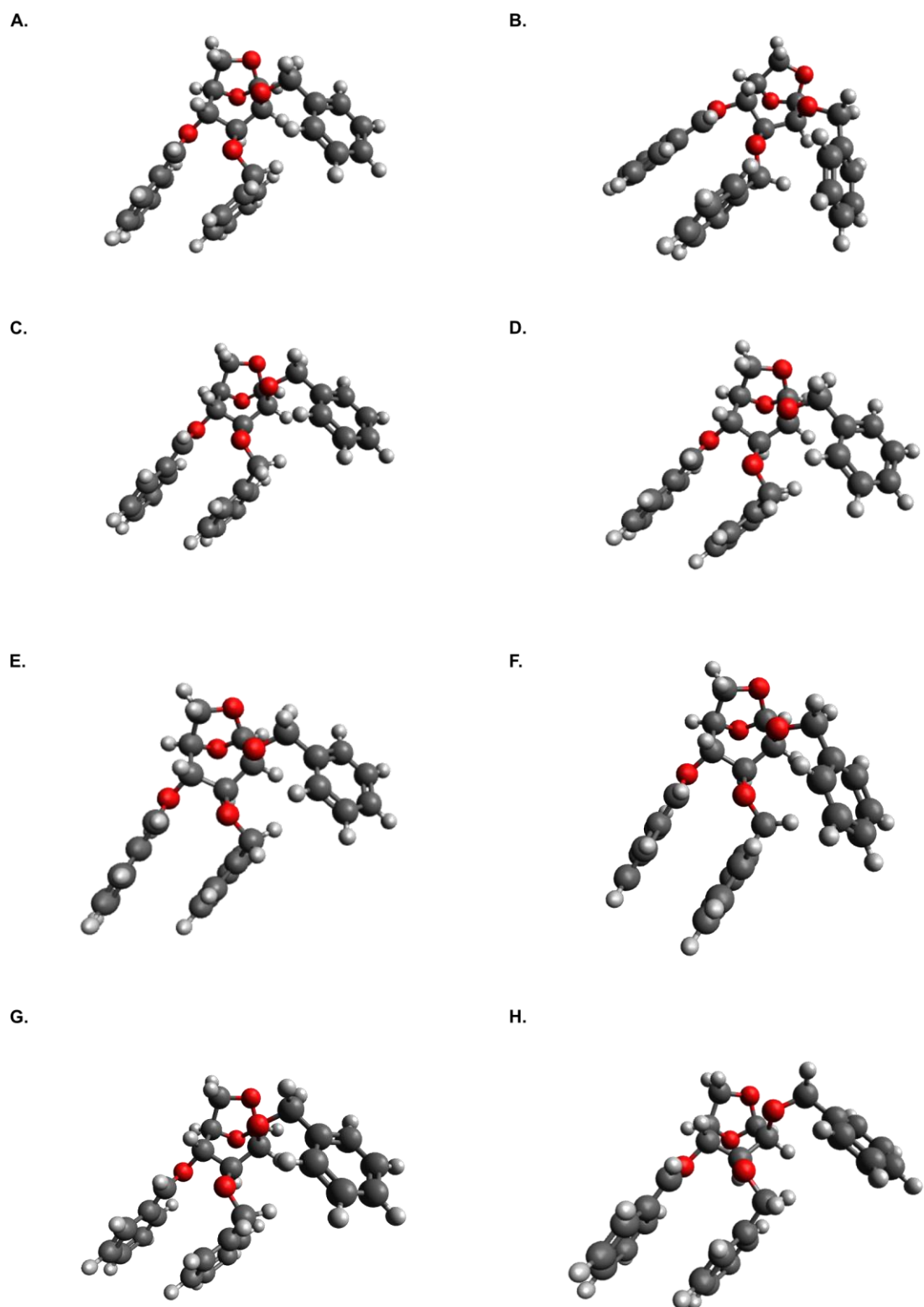


Figure S20. Reoptimized geometries of **Man-6B** within different surrounding medias (solvents). The structures correspond to those that are highlighted in entry 1, **Error! Reference source not found.** A) 1,4-Dioxane. B) Toluene. C) Et₂O. D) CHCl₃. E) DCM. F) ACN. G) DMSO. H) Water.

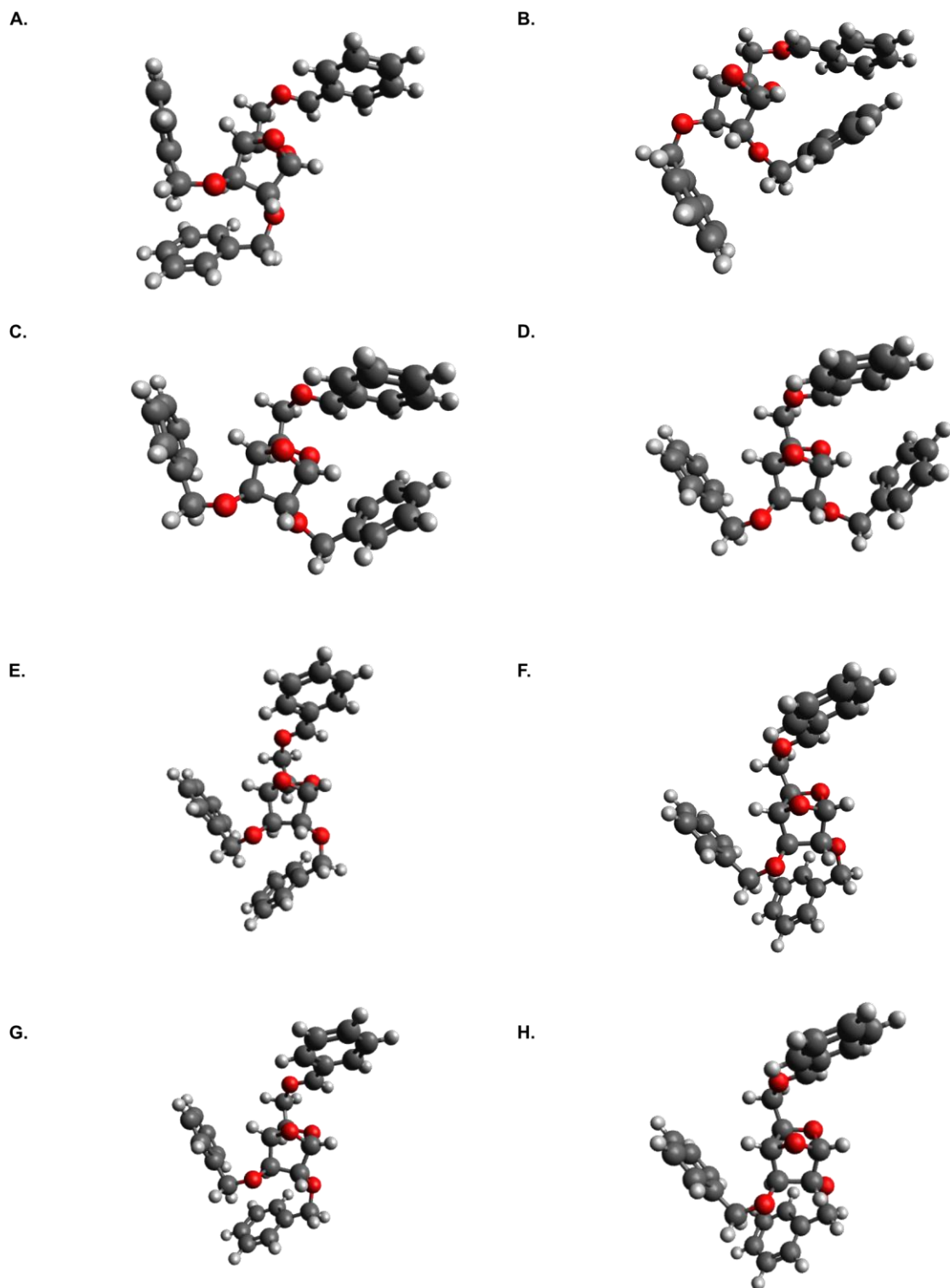


Figure S21. Reoptimized geometries of **Gal-4B** within different surrounding medias (solvents). The structures correspond to those that are highlighted in entry 1, **Error! Reference source not found.** A) 1,4-Dioxane. B) Toluene. C) Et₂O. D) CHCl₃. E) DCM. F) ACN. G) DMSO. H) Water.

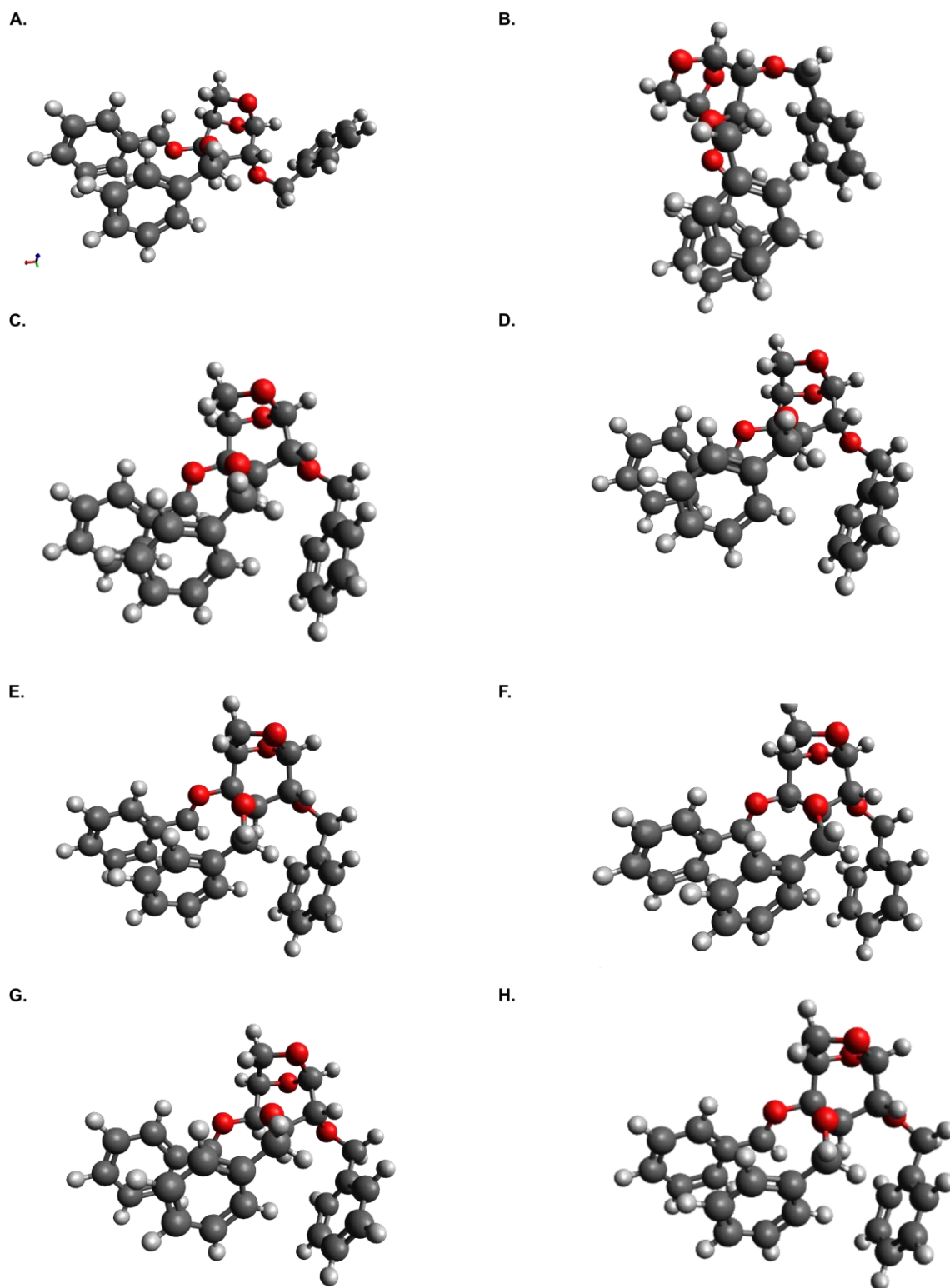


Figure S22. Reoptimized geometries of **Gal-6B** within different surrounding medias (solvents). The structures correspond to those that are highlighted in entry 1, **Error! Reference source not found.** A) 1,4-Dioxane. B) Toluene. C) Et₂O. D) CHCl₃. E) DCM. F) ACN. G) DMSO. H) Water.

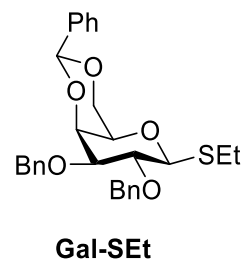
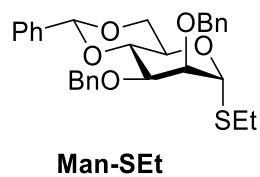
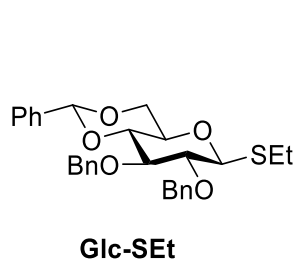
2.8 xyz-Coordinates of Reoptimized Structures

xyz-Coordinates of all reoptimized geometries at the PBE0+D3/6-311+G(d,p) level of theory can be found in a separate document “SI_Coordinates_gas phase.pdf” and “SI_Coordinates_within solvents.pdf”.

3. Experimental Details

3.1 Materials

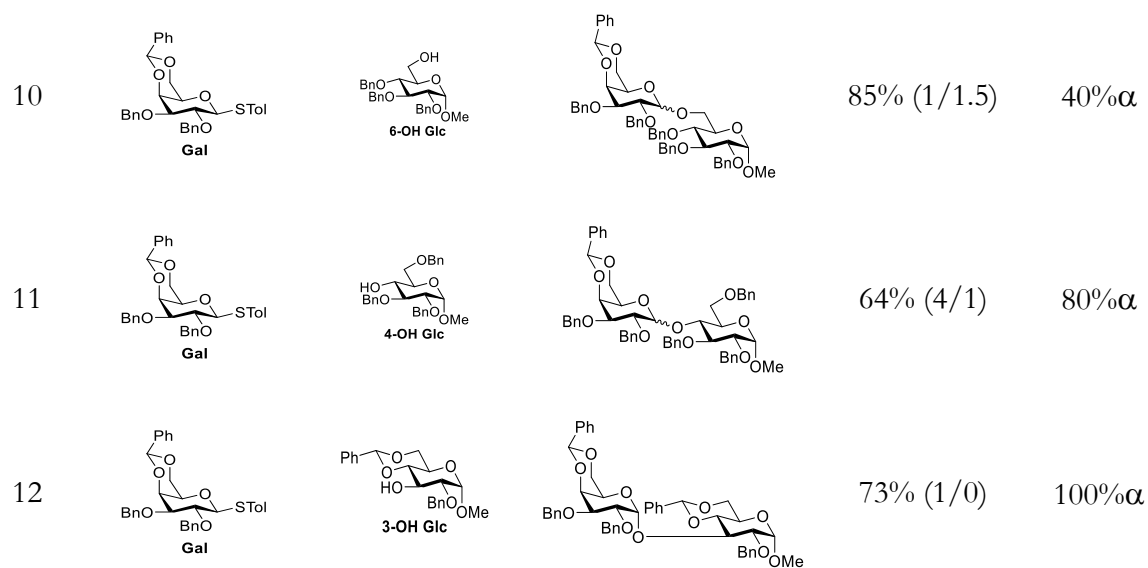
Ethyl thioglycoside donors were selected as the precursor for mass spectrometry and cryogenic IR experiments. Synthesis and spectroscopic data of Glc-SEt⁹, Gal-SEt¹⁰, Man-SEt¹¹ can be found in the cited references.



3.2 Probing the Stereoselectivity of 4,6-*O*-Benzylidene-Directed Glycosylation Reaction

Table S7. Glycosylation Reaction in NIS/TfOH promotor System.

$ \begin{array}{c} \text{Ph} \\ \diagup \quad \diagdown \\ \text{O} \quad \text{O} \\ \diagdown \quad \diagup \\ \text{BnO} \quad \text{BnO} \quad \text{STol} \end{array} + \text{Acceptor} \xrightarrow[\text{DCM, -40 } ^\circ\text{C, 3 h}]{\text{NIS (1.0 equiv.), TfOH (0.3 equiv.)}} \begin{array}{c} \text{Ph} \\ \diagup \quad \diagdown \\ \text{O} \quad \text{O} \\ \diagdown \quad \diagup \\ \text{BnO} \quad \text{BnO} \quad \text{OR} \end{array} $					
Entry	Donor	Acceptor	Product	Yield ^a (α/β) ^b	α -ratio (%)
1		MeOH		79% (1/4)	25% α
2				70% (1/1)	50% α
3				60% (1/1)	50% α
4				44% (1/1)	50% α
5		MeOH		70% (1/5)	17% α
6				66% (1/2)	33% α
7				58% (1/1.4)	42% α
8				45% (1/1.7)	37% α
9		MeOH		53% (1/4)	20% α



^aIsolated yield. ^b Determined by HPLC. The examples of glycosylation reaction in condensed phase (showed below) is obtained from the report by Wang et al..^{12,13}

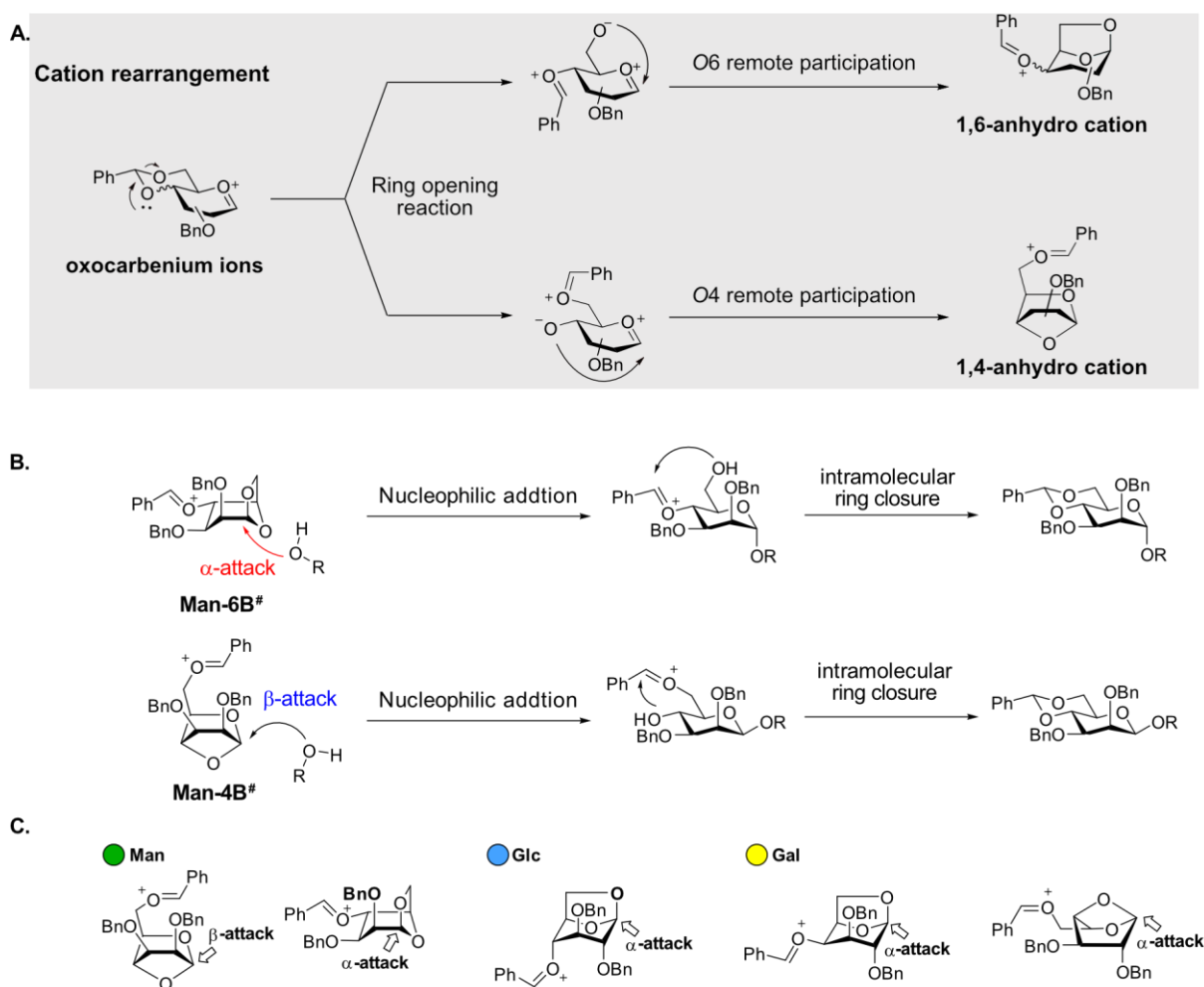


Figure S23. Hypothetical S_N1 -mechanism of 4,6-benzylidene-mediated glycosylation of the gas-phase intermediates. A) Activation of glycosyl donors leads to oxocarbenium ions, which subsequently undergoes a ring opening reaction of the benzylidene acetal at O4 and O6.¹⁴ Next, remote participation¹⁵ of the ether at O6 or O4 occurs to give the energetically more stable 1,6-anhydro or 1,4-anhydro cations, as confirmed by cryogenic IR spectroscopy. B) For mannosylations, both **Man-6B** and **Man-4B** can be generated and have inverse selectivities, potentially explaining the mixed ratios observed in its S_N1 -type glycosylations. **Man-4B** promotes the attack of the acceptor from the β -face, whereas **Man-6B** blocks the upper side, resulting in α -nucleophilic addition. C) The inverse selectivities of the anhydro cations correlates well with the mixed anomer ratios that are often observed when benzylidene-protected donors are used under conditions that favor an S_N1 -type glycosylation reaction.

References

- (1) Schöllkopf, W.; Gewinner, S.; Junkes, H.; Paarmann, A.; von Helden, G.; Bluem, H. P.; Todd, A. M. M. The new IR and THz FEL facility at the Fritz Haber Institute in Berlin. *Proc. SPIE Int. Soc. Opt. Eng.* **2015**, *9512*, 95121L.
- (2) Gaussian 16, Revision C.01, M. J. Frisch, G. W. Trucks, H. B. Schlegel, G. E. Scuseria, M. A. Robb, J. R. Cheeseman, G. Scalmani, V. Barone, G. A. Petersson, H. Nakatsuji, X. Li, M. Caricato, A. V. Marenich, J. Bloino, B. G. Janesko, R. Gomperts, B. Mennucci, H. P. Hratchian, J. V. Ortiz, A. F. Izmaylov, J. L. Sonnenberg, D. Williams-Young, F. Ding, F. Lipparini, F. Egidi, J. Goings, B. Peng, A. Petrone, T. Henderson, D. Ranasinghe, V. G. Zakrzewski, J. Gao, N. Rega, G. Zheng, W. Liang, M. Hada, M. Ehara, K. Toyota, R. Fukuda, J. Hasegawa, M. Ishida, T. Nakajima, Y. Honda, O. Kitao, H. Nakai, T. Vreven, K. Throssell, J. A. Montgomery, Jr., J. E. Peralta, F. Ogliaro, M. J. Bearpark, J. J. Heyd, E. N. Brothers, K. N. Kudin, V. N. Staroverov, T. A. Keith, R. Kobayashi, J. Normand, K. Raghavachari, A. P. Rendell, J. C. Burant, S. S. Iyengar, J. Tomasi, M. Cossi, J. M. Millam, M. Klene, C. Adamo, R. Cammi, J. W. Ochterski, R. L. Martin, K. Morokuma, O. Farkas, J. B. Foresman, and D. J. Fox, Gaussian, Inc., Wallingford CT. **2016**.
- (3) Pracht, P.; Bohle, F.; Grimme, S. Automated Exploration of the Low-energy Chemical Space with Fast Quantum Chemical Methods. *Phys. Chem. Chem. Phys.* **2020**, *22*, 7169-7192.
- (4) Bannwarth, C.; Ehlert, S.; Grimme, S. GFN2-xTB—An Accurate and Broadly Parametrized Self-Consistent Tight-Binding Quantum Chemical Method with Multipole Electrostatics and Density-Dependent Dispersion Contributions. *J. Chem. Theory Comput.* **2019**, *15*, 1652-1671.
- (5) Adamo, C.; Barone, V. Toward reliable density functional methods without adjustable parameters: The PBE0 model. *J. Chem. Phys.* **1999**, *110*, 6158-6170.
- (6) Grimme, S.; Antony, J.; Ehrlich, S.; Krieg, H. A consistent and accurate ab initio parametrization of density functional dispersion correction (DFT-D) for the 94 elements H-Pu. *J. Chem. Phys.* **2010**, *132*, 154104.

- (7) Klamt, A.; Schüürmann, G. COSMO: a new approach to dielectric screening in solvents with explicit expressions for the screening energy and its gradient. *J. Chem. Soc., Perkin Trans. 2* **1993**, 799-805.
- (8) Warnke, S.; Seo, J.; Boschmans, J.; Sobott, F.; Scrivens, J. H.; Bleiholder, C.; Bowers, M. T.; Gewinner, S.; Schollkopf, W.; Pagel, K.; von Helden, G. Protomers of Benzocaine: Solvent and Permittivity Dependence. *J. Am. Chem. Soc.* **2015**, *137*, 4236-4242.
- (9) Crich, D.; de la Mora, M.; Vinod, A. U. Influence of the 4,6-O-Benzylidene, 4,6-O-Phenylboronate, and 4,6-O-Polystyrylboronate Protecting Groups on the Stereochemical Outcome of Thioglycoside-Based Glycosylations Mediated by 1-Benzenesulfinyl Piperidine/Triflic Anhydride and N-Iodosuccinimide/Trimethylsilyl Triflate. *J. Org. Chem.* **2003**, *68*, 8142-8148.
- (10) Hahm, H. S.; Hurevich, M.; Seeberger, P. H. Automated assembly of oligosaccharides containing multiple cis-glycosidic linkages. *Nat. Commun.* **2016**, *7*, 12482.
- (11) Crich, D.; Smith, M. 1-Benzenesulfinyl Piperidine/Trifluoromethanesulfonic Anhydride: A Potent Combination of Shelf-Stable Reagents for the Low-Temperature Conversion of Thioglycosides to Glycosyl Triflates and for the Formation of Diverse Glycosidic Linkages. *J. Am. Chem. Soc.* **2001**, *123*, 9015-9020.
- (12) Chang, C.-W.; Wu, C.-H.; Lin, M.-H.; Liao, P.-H.; Chang, C.-C.; Chuang, H.-H.; Lin, S.-C.; Lam, S.; Verma, V. P.; Hsu, C.-P.; Wang, C.-C. Establishment of Guidelines for the Control of Glycosylation Reactions and Intermediates by Quantitative Assessment of Reactivity. *Angew. Chem. Int. Ed.* **2019**, *58*, 16775-16779.
- (13) Chang, C.-W.; Lin, M.-H.; Chan, C.-K.; Su, K.-Y.; Wu, C.-H.; Lo, W.-C.; Lam, S.; Cheng, Y.-T.; Liao, P.-H.; Wong, C.-H.; Wang, C.-C. Automated Quantification of Hydroxyl Reactivities: Prediction of Glycosylation Reactions. *Angew. Chem. Int. Ed.* **2021**, *60*, 12413-12423.
- (14) Kirschbaum, C.; Greis, K.; Polewski, L.; Gewinner, S.; Schöllkopf, W.; Meijer, G.; von Helden, G.; Pagel, K. Unveiling Glycerolipid Fragmentation by Cryogenic Infrared Spectroscopy.

J. Am. Chem. Soc. **2021**, *143*, 14827-14834.

(15) Marianski, M.; Mucha, E.; Greis, K.; Moon, S.; Pardo, A.; Kirschbaum, C.; Thomas, D. A.; Meijer, G.; von Helden, G.; Gilmore, K.; Seeberger, P. H.; Pagel, K. Remote Participation during Glycosylation Reactions of Galactose Building Blocks: Direct Evidence from Cryogenic Vibrational Spectroscopy. *Angew. Chem. Int. Ed.* **2020**, *59*, 6166-6171.